Enhancement of optical processes in coupled plasmonic nanocavities [Invited]

Patrice Genevet,[1,2] Jean-Philippe Tetienne,[1] Romain Blanchard,[1] Mikhail A. Kats,[1] J. P. Balthasar Müller,[1] Marlan O. Scully,[2,3] and Federico Capasso[1,*]

[1]School of Engineering and Applied Sciences, Harvard University, Cambridge, Massachusetts 02138, USA

[2]Institute for Quantum Studies and Department of Physics, Texas A&M University, College Station, Texas 77843, USA

[3]College of Engineering and Applied Science, Princeton University, Princeton, New Jersey 08544, USA

*Corresponding author: capasso@seas.harvard.edu

Received 11 July 2011; accepted 2 August 2011;
posted 15 August 2011 (Doc. ID 150601); published 11 October 2011

We present detailed experimental and numerical investigations of resonances in deep nanogroove gratings in metallic substrates. These plasmonic nanocavity gratings feature enhanced fields within the grooves that enable a large enhancement of linear and nonlinear optical processes. This enhancement relies on both localized and propagating surface plasmons on the nanopatterned surface. We show that the efficiency of optical processes such as Raman scattering and four-wave mixing is dramatically enhanced by plasmonic nanocavity gratings.

OCIS codes: 240.4350, 190.4380.

1. Introduction

The unique optical properties of metallic nanostructures have recently attracted a great deal of attention, bringing the field of plasmonics [1,2] to the forefront of nanophotonics research. Plasmonic elements have led to applications in optical labeling [3] and chemical and biological sensing [4,5], and more recently have enabled the utilization of nonlinear optical processes at the nanoscale [6–11].

In this paper, we demonstrate that plasmonic nanocavity gratings [11] can be used as substrates for enhancement of different types of optical processes. Plasmonic nanocavity gratings consist of deep periodically arranged grooves patterned into metallic films to create resonant nanocavities [12,13] at desired frequencies. Such structures take advantage of the excitation of surface waves, known as surface plasmon polaritons, via a second order grating to funnel and concentrate the energy into highly localized plasmonic modes of the nanocavities (see Fig. 1).

0003-6935/11/310G56-07$15.00/0

In the first part of this paper, we will discuss the resonant properties of our plasmonic nanocavity gratings. Supported by finite-difference time-domain simulations (FDTD Lumerical solutions) we show that the maximum field enhancement in the groove is obtained when the structure satisfies a double resonance condition, i.e., when the grating launches surface waves at a wavelength that is also resonant with the localized cavity mode. The second part of this paper is devoted to showing the potential of our structure for enhancing optical processes. We experimentally demonstrate enhanced nonlinear four-wave mixing (4 WM) and Raman scattering in plasmonic nanocavity gratings.

2. Resonances of Coupled Plasmonic Nanocavities

The optical properties of the structure sketched in Fig. 1 can be analyzed by using FDTD simulations. Figures 2(a)–2(c) summarize the resonance properties of plasmonic nanocavity gratings.

Fig. 2(a) shows the intensity, measured in the center of the groove entrance (denoted by the small x in the inset) and normalized by the incident intensity $|E/E_0|^2$, for a single nanocavity. This plot shows that

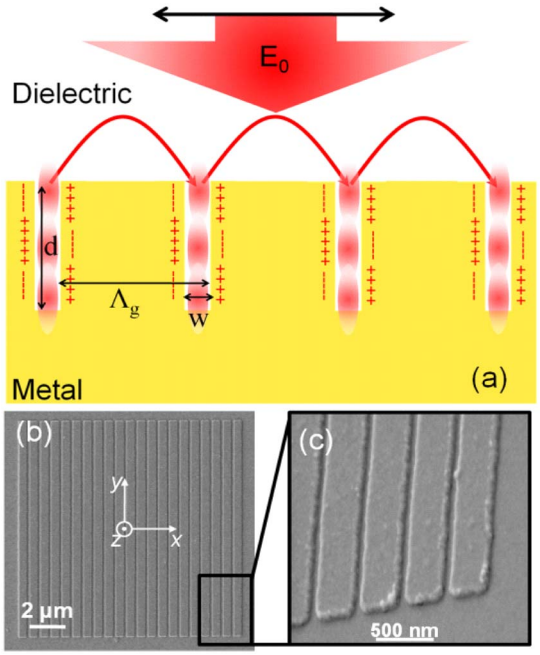

Fig. 1. (Color online) (a) Schematic of a plasmonic nanocavity grating consisting of deep periodically arranged nanogrooves patterned in a metallic film, which couple incident free space light into surface waves. Surface waves subsequently funnel energy into the resonant modes of the nanocavities, considerably increasing the electromagnetic energy stored in the nanocavity modes. (b),(c) Scanning electron microscopy images of the fabricated structures.

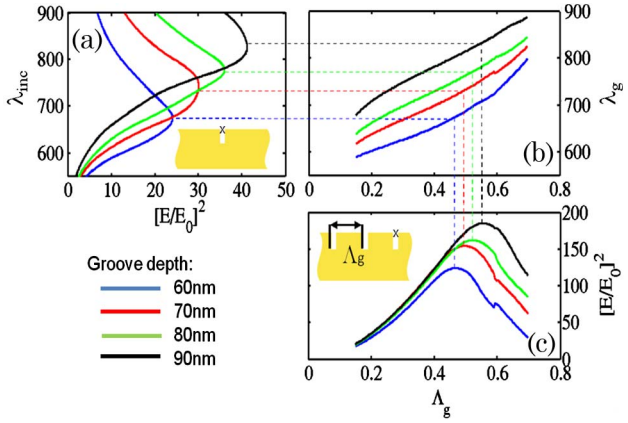

Fig. 2. (Color online) (a) Simulation of the resonances of an isolated single nanocavity with depth d ranging from 60 to 90 nm. The resonance peak is controlled by the depth of the groove. (b) Calculation of the position of the resonance peak for plasmonic nanocavity gratings as a function of the grating period. Grating launches surface Plasmon waves at a wavelength ($\lambda_g = \lambda_{\mathrm{inc}} = n_{\mathrm{eff}}$) that depends linearly on the grating period. (c) We extract from the resonance curves the maximum of the electric field enhancement and plot it as a function of the grating period Λ_g. For each nanocavity depth, there is an optimal Λ_g that maximizes the field enhancement produced by the structure. The position of the maximum enhancement occurs when $\lambda_{\mathrm{inc}} = n_{\mathrm{eff}}\Lambda_g = \lambda_{\mathrm{cav}}$. By changing Λ_g, the double resonance condition is lost, resulting in a decreased field enhancement in the grooves. For all simulations, a focused Gaussian beam with a 1 μm waist size and wavelength λ_{inc} is impinging onto the structure at normal incidence. The electric field is measured at the center of the groove entrance (denoted by the x in the inset), and is normalized to that of the incident wave. n_{eff} is the effective mode index of the surface waves propagating at the corrugated interface.

the resonance wavelength (λ_{cav}) of the nanocavity is controlled by the depth d. Increasing d red-shifts the resonance of the nanostructure. This behavior is explained by considering the nanocavities as truncated vertical metal-insulator-metal waveguides [14] for which the bottom part is replaced by a gold mirror and the upper part is open to the air. This causes the nanocavities to behave as nanoscale Fabry–Perot resonators.

Figure 2(b) presents the calculated position λ_g of the maximum of resonance for plasmonic nanogroove gratings as a function of the grating period Λ_g. Note that for a given d and a fixed incidence angle (α), Λ_g controls the wavelength of the coupled surface wave, i.e., such that

$$k_0 \sin(\alpha) + q\beta_g = k_g, \tag{1}$$

where q is an integer, $\beta_g = 2\pi/\Lambda_g$, $k_g = n_{\mathrm{eff}}k_0$ and k_0 are the wave vector of the surface wave and of the free-space wave vector, respectively, and n_{eff} is the effective mode index of the waves propagating along the nanogroove grating surface.

For a given Λ_g but at different d, we observe that the coupled wavelength changes. This indicates that both d and Λ_g contribute to the resonance of the system. In Fig. 2(c), we plot the maximum of the normalized electromagnetic field as a function of Λ_g. We observe that the maximum field at the groove entrance is obtained when Λ_g is such that the grating launches surface waves, which are resonant with the intrinsic mode of the isolated nanocavities, i.e., when $\lambda_{\mathrm{inc}} = n_{\mathrm{eff}}\Lambda_g = \lambda_{\mathrm{cav}}$. In this case, the incident light coupled into the localized nanocavity modes is assisted by surface plasmon polaritons propagating at the surface of the corrugated metallic structure. For practical applications, once the operating wavelength has been determined, the depth of the nanocavities can be chosen. Then, to maximize the field enhancement produced by the structure, for a given incident angle, the grating period must be chosen to launch surface waves that are also resonant with the intrinsic nanocavity modes (λ_{cav}), i.e., which satisfy Eq. (1) with $k_g = 2\pi n_{\mathrm{eff}}/\lambda_{\mathrm{cav}}$.

Note that the number of illuminated grooves plays an important role in this coupling process. By increasing the beam waist, a larger number of grooves are simultaneously illuminated, thereby narrowing the resonance and improving the coupling to surface waves.

To better characterize the influence of the geometrical parameter (w, d, Λ_g) of the patterned structure on the electromagnetic field, we introduce the local field enhancement factor η_{in}.

Fig. 3 shows the two different procedures employed to evaluate this local enhancement factor η_{in}, for a given frequency, in the air ($\eta_{\mathrm{in,air}}$) and in

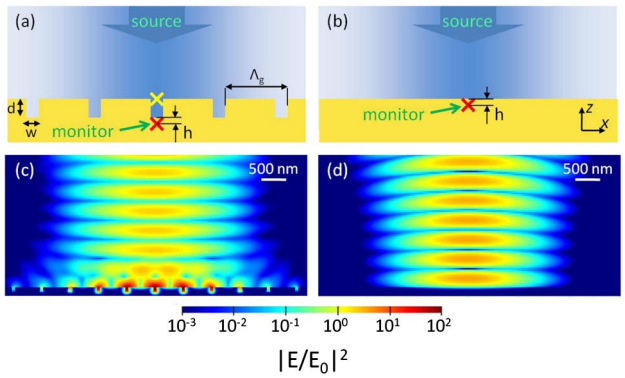

Fig. 3. (Color online) The local enhancement factor (η_{in}) in the metal and in the gap of the nanocavity is calculated as follows: At the groove entrance at the location indicated by the yellow cross in (a), $\eta_{\text{in,air}} = |E/E_0|$, where the calculated field E is normalized to the incident field E_0. In the metal, we must account for the finite penetration, i.e., the skin depth of the electromagnetic field. We therefore define $\eta_{\text{in,metal}} = |E/E_{\text{flat,metal}}|$ where the field E calculated at the location indicated by the red cross in (a) is normalized to the field $E_{\text{flat,metal}}$ of the unpatterned structure [red cross in (b)]. Electric field distribution $|E/E_0|^2$ for a nanogroove grating with a width $w = 60\,\text{nm}$, a depth $d = 90\,\text{nm}$ and $\Lambda_g = 560\,\text{nm}$ (c), and for a flat gold surface (d). The incident Gaussian beam has a maximum field amplitude $|E_0|$ and a free space wavelength $\lambda_{\text{inc}} = 820\,\text{nm}$.

the metal ($\eta_{\text{in,metal}}$) considering a normally incident Gaussian beam polarized along x, with a $1\,\mu\text{m}$ waist size.

In the next section, we will make use of these enhancement factors to quantify the influence of the geometrical parameters of the structure (w, d, and Λ_g) on the generated nonlinear four wave mixing signal and on the Raman scattering signal.

3. Plasmonic Nanocavity Gratings Enhance Optical Processes

A. Four-Wave Mixing

Noble materials have intrinsically large nonlinear coefficients, notably their third order susceptibility $\chi^{(3)}$, which, for example, for gold films can be about 10 times higher than that of $LiNO_3$ ([15]). We have previously reported that an enhanced 4 WM signal can be obtained in gold plasmonic nanocavities [11]. In the following, we would like to elaborate on the method used to design the plasmonic structure for 4 WM and the role of η in the enhancement of this nonlinear process. Since the nonlinear material used for this experiment is the gold itself, for simplicity we will omit the subscript "metal" in the next section. In this process, two photons at ω_1 interact with a photon at ω_2 to generate a nonlinear polarization at $\omega_{4\,\text{WM}}$ such that $\omega_{4\,\text{WM}} = 2\omega_1 - \omega_2$. This nonlinear process, known as degenerate up-converted 4 WM, occurs in the vicinity of plasmonic structures where the fields exhibit plasmonic enhancement and where the generated nonlinear polarization undergoes coherent scattering by the structure. The plasmonic field enhancement experienced by each beam can be directly characterized via the η_{in} at each frequency. Because of Purcell enhancement, collimation effect by the structure, and the finite numerical aperture of the microscope objective used for the experiment, there is an enhancement of the collected 4 WM signal with respect to one coming from a flat surface [16,17]. To better characterize both this emission enhancement and the coherent scattering of the generated polarization, we introduce the out-coupling enhancement factor (η_{out}) of the structure, which quantifies the influence of the environment on the emission of a small volume of polarized medium emitting at a given frequency. This volume is modeled as an electric dipole. The dipole is aligned along x, i.e., along the dimension perpendicular to the grooves, and positioned like the monitors used to evaluate η_{in}, i.e., within the metal at a distance $h = 5\,\text{nm}$ below the air/metal interface (red crosses in a and b). We monitor the radiated field and calculate the power P_{rad}, which would be collected by a microscope objective (we assume a 40× microscope objective with 0.75 NA). $P_{\text{rad,flat}}$ can be obtained in the same manner for a flat surface, from which $\eta_{\text{out}} = P_{\text{rad}}/P_{\text{rad,flat}}$ is deduced.

An example of the simulation is shown in Figs. 4(c) and 4(d). An electric dipole located beneath the flat surface both radiates in the far field and excites freely propagating surface plasmon polaritons (Fig. 4(d).) The case of a nanogroove grating is very different (Fig. 4(c).) The dipole source also launches surface waves on the corrugated surface, but as they propagate away from the source they undergo coherent scattering at the grooves. The direction of constructive interference (angle with respect to the normal to the surface) is then determined by Eq. (1). For instance, with grooves of 90 nm depth and 60 nm gap, light is emitted mainly normal to the surface ($= 0$) when the grating period is $\Lambda_g = 300\,\text{nm}$ at $\lambda = 670\,\text{nm}$ and $q = 1$.

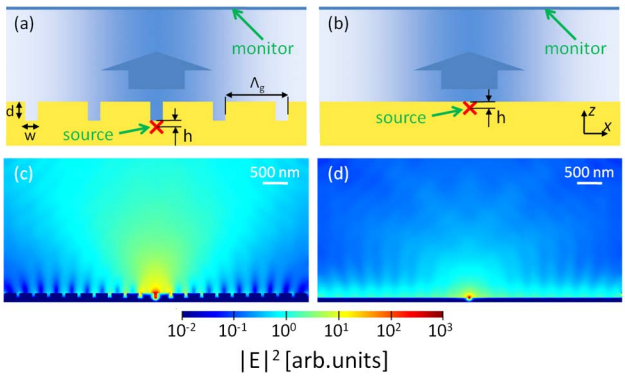

Fig. 4. (Color online) The out-coupling enhancement factor $\eta_{\text{out}} = P_{\text{rad}}/P_{\text{rad/flat}}$ is calculated from the power P_{rad} radiated by an electric dipole of moment p aligned along x in a patterned structure [red cross in (a)], normalized to the power $P_{\text{rad/flat}}$ radiated by the same dipole in an unpatterned structure [red cross in (b)]. Intensity distribution $|E|^2$ for a nanogroove grating with $w = 60\,\text{nm}$, $d = 90\,\text{nm}$, and $\Lambda_g = 300\,\text{nm}$ (c), and for a flat gold surface (d). The electric dipole is oscillating at the frequency corresponding to the free space wavelength $\lambda = 670\,\text{nm}$.

After defining enhancement factors at each frequency, we can estimate the overall enhancement of such a complex nonlinear process by defining the local 4 WM enhancement factor: $EF_{local} = \eta_{in,1}^4 \eta_{in,2}^2 \eta_{out,4WM}^2$. Since the η's are obtained using either point monitors or point sources, the EF_{local} is a local value. This local EF_{local} can also be obtained by $EF_{local} = P_{4\,WM,local}/P_{4\,WM,flat,local}$, where $P_{4\,WM,local}$ and $P_{4\,WM,flat,local}$, are the powers collected at $\omega_{4\,WM}$ when the patterned and unpatterned gold structures, respectively, are illuminated by two beams at frequencies ω_1 and ω_2, considering only an infinitesimal volume of gold where the nonlinear polarization is generated. The infinitesimal volume, modeled by a single dipole, is centered around the location of the red cross monitor in Fig. 3 and around the source in Fig. 4. The overall 4 WM enhancement could be in principle calculated by summing the 4 WM fields generated by each volume element of the gold structure, normalized to the result of the same summation for a flat surface. However, performing such a summation with FDTD simulations remains challenging. We therefore cannot directly compare the overall 4 WM enhancement to EF_{local}. However, we expect that the dependence on the geometrical parameters is similar for both local and overall enhancements, especially because our experiments have been performed with a relatively high NA microscope objective—the incident beam has a $\sim 1\,\mu$m waist size—for which the volume of interaction is limited to the waist of the beam, thereby limiting interference effects which might occurs when considering a spatial distribution of sources for the 4 WM polarization.

Figure 5 shows $\eta_{in,1}^2$ and $\eta_{in,2}^2$ as a function of d and Λ_g, respectively. These colorplots enable us to quantify the combined effect of localized surface plasmons and surface waves on the field enhancement and on the in-coupling process. $\eta_{in,1}^2$ vs. d exhibits a maximum when there exists a resonant mode at λ_{inc}, i.e., when d is such that $\lambda_{inc} = \lambda_{cav}$. At the same time, $\eta_{in,1}^2$ vs. Λ_g exhibits a maximum when the surface waves at ω_{inc} are efficiently excited, i.e., when Λ_g is such that $\lambda_{inc} = n_{eff} m \Lambda_g$ (m is an integer). The same arguments also apply for $\eta_{in,2}^2$ vs. d and Λ_g, but since the incident frequency is different, the double resonance condition is reached for a different set of geometrical parameters. The maxima in Fig. 5 correspond to $m = 1$.

We can also display the calculated $\eta_{out,4\,WM}$ as a function of d and Λ_g (Fig. 6). This plot enables us to observe again the role of both nanocavity modes and the surface waves on the field enhancement in the out-coupling process. As for the in-coupling mechanism, $\eta_{out,4\,WM}$ vs. d exhibits a maximum when there exists a nanocavity mode at λ_{dipole}, i.e., when d is such that $\lambda_{dipole} = \lambda_{cav}$. Also here, at the same time, $\eta_{out,4\,WM}$ vs. Λ_g exhibits a maximum when the surface waves at λ_{dipole}, are efficiently converted into photons that are able to reach the detector, i.e., when Λ_g is such that $\lambda_{dipole} = m n_{eff} \Lambda_g$ (m is an integer). The maxima in Fig. 6 correspond to $m = 1$, $m = 2$, and $m = 3$, respectively. Because $\eta_{in,1}$ appears at the fourth power in the expression for EF_{local}. it is clear that the maximum enhancement factor of the whole nonlinear process would occur for devices designed to maximize $\eta_{in,1}$. To do so, we fabricated and measured arrays of nanocavity gratings that achieve localized resonance at ω_1, i.e,. for 90 nm deep nanocavities (see Fig. 5(a)).

Fig. 7 shows a schematic of the experimental setup used to measure the enhanced 4 WM signal. Mode-locked laser pulse-trains at 820 nm (λ_1) are generated by an optical parametric oscillator (Levante Emerald, APE-Berlin) synchronously pumped by a frequency doubled Nd:YVO4 laser (picoTRAIN, High-Q $\lambda =$ 532 nm, 7 ps pulse duration, 76 MHz repetition rate). Additionally, the pump laser provides another output at 1064 nm (λ_2). Since many of the optical components inserted along the beam paths are polarization-sensitive, we fixed the polarization of both beams and mounted the sample on a rotation stage to align the polarization of both laser beams perpendicular to the grooves (for such incident polarization, the coupling between incident TE to TM surface waves is maximized [18]). The two beams are spatially and temporally overlapped before being sent into an inverted Olympus FV 300 confocal microscope through a scanning module. The scanning module is composed of two mirrors acting on two spatial dimensions and enables us to scan the sample along x and y. Light is focused onto the sample using a 40× objective (0.75 NA). For such an objective, the scanning area is about 350 μm by 350 μm. The generated 4 WM light

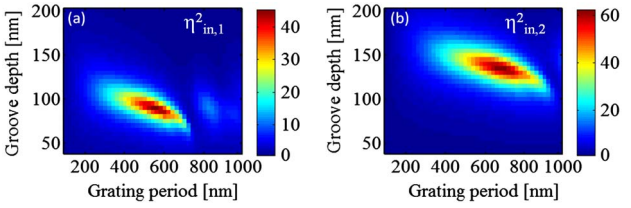

Fig. 5. (Color online) (a),(b) Calculated local enhancement factor $\eta_{in,1}$ at ω_1 and $\eta_{in,2}$ at ω_2 (b) as a function of d and Λ_g for normally incident monochromatic laser beams focused on the nanocavity grating. The simulated groove width is $w = 60$ nm. In (a) and (b) the incident free space wavelength is 820 nm and 1064 nm, respectively.

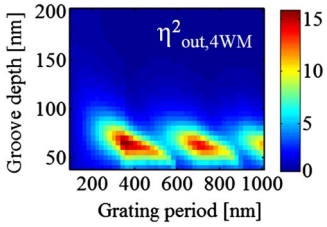

Fig. 6. (Color online) Calculated local enhancement factor $\eta_{out,4\,WM}$ at $\omega_{4\,WM}$ as a function of d and Λ_g. The simulated groove width is $w = 60$ nm. In our experiment, we only considered the up-converted four wave mixing signal which results in light generation at 667 nm. The dipole used for this simulation is emitting at this wavelength noted λ_{dipole} in the text.

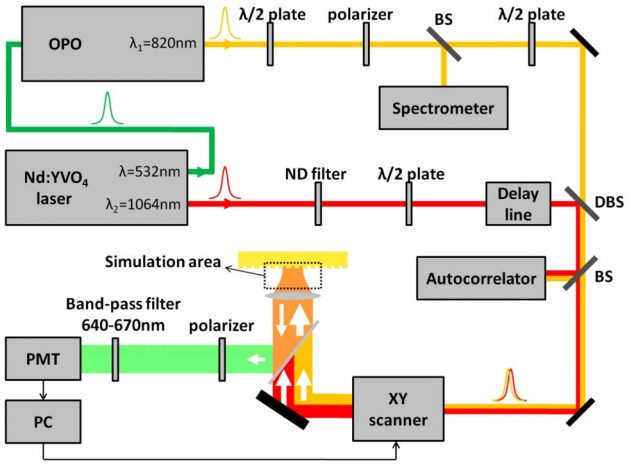

Fig. 7. (Color online) Schematic of the experimental setup. It consists in a typical coherent anti-Stokes Raman scattering microscope. BS stands for beamsplitter, DBS for dichroic beam splitter, ND for neutral density. A computer (PC) controls the XY scanning while it records the signal from the photomultiplier (PMT) module.

is collected through the same objective, separated from the incident light by a dichroic beam splitter, filtered, and detected by a photomultiplier. Collecting the 4 WM signal as a function of the beam position allows us to create an intensity map of a sample that contains several $13\,\mu\text{m} \times 13\,\mu\text{m}$ gratings with different geometrical parameters. Gratings are fabricated by e-beam lithography on a silicon substrate followed by e-beam evaporation of gold. After the liftoff, a second e-beam evaporation of gold creates a fully metalized structure. We note that the study of nonlinear optical phenomena often requires intense laser pulses that can deteriorate the nanostructure, especially for high repetition rates as is the case in our experiment. The second evaporation helps with thermal management and prevents damage to the structure by creating a continuous thermally conductive layer.

Figure 8(a) presents the experimental measurements of the 4 WM enhancement as a function of the grating period Λ_g for a fixed depth and width of the nanocavities ($d = 90\,\text{nm}$, $w = 80\,\text{nm}$). Each mark in Fig. 8(a) corresponds to the detected 4 WM signal from few grooves (ranging between 2 to maximum 10 depending Λ_g), averaged over the corresponding grating and normalized by that of a flat gold interface to express the enhancement factor ($\text{EF}_{\text{measured}} = P_{4\,\text{WM,measured}}/P_{4\,\text{WM,flat,measured}}$). We remark that the maximum enhancement occurs for $\Lambda_g = 560\,\text{nm}$, i.e., when $\eta_{\text{in1,metal}}$ is maximum (see Fig. 5(a).) Fig. 8(b) shows the calculated local nonlinear polarization enhancement for the corresponding structure $|\eta_{\text{in},1}|^4|\eta_{\text{in},2}|^2$. We also remark that the local maximum of the 4 WM signal at $\Lambda_g \sim 320\,\text{nm}$ corresponds to the position of the peak of the calculated out-coupling coefficient ($|\eta_{\text{out},4\,\text{WM}}|^2$). The validity of the previous argument that local enhancement factors can help to understand the total enhancement factor of the nonlinear process is confirmed by comparing the position of the maximum of the calculated local nonlinear polarization with that of the maximum of the 4 WM signal as a function of Λ_g. As was expected with the simulation, a maximum of nonlinear four wave mixing enhancement, of about 2000, occurs for plasmonic nanocavity grating exhibiting a double resonance condition at λ_1. We recall that the measured 4 WM enhancement results from the summation of the 4 WM fields generated by each volume element of the gold structure and therefore may differ from the multiplication of the local enhancement factors in Figs. 8(b) and 8(c).

B. Surface Enhanced Raman Scattering

Figure 9 presents the results obtained on the surface enhanced Raman scattering (SERS) measurements from a self-assembled monolayer of benzenethiol molecules adsorbed on silver-based plasmonic nanocavity gratings. Figure 9(a) sketches the experiment: a ~5 mW pump laser beam at 532 nm with an incident polarization perpendicular to the grooves is focused onto the structure using the 20× microscope objective of a Witec confocal Raman microscope. The Raman scattered (Stokes) signal and the reflected pump beam are collected together via the same objective. The Raman signal is separated from the pump light by a filter and then directly fed in a spectrometer to acquire the Raman spectrum. For this experiment, the plasmonic structure is specifically designed in silver (Ag) to avoid non-desirable interband transitions that take place in gold for our pumping wavelength of 532 nm. To avoid any oxidation of the Ag

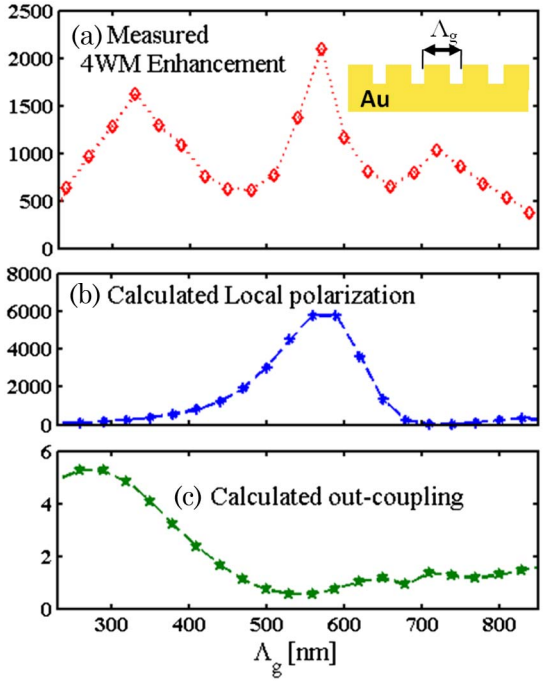

Fig. 8. (Color online) (a) Measured 4 WM signal enhancement as a function of grating period Λ_g. (b) Calculated local nonlinear polarization enhancement $|\eta_{\text{in},1}|^4|\eta_{\text{in},2}|^2$ as a function of Λ_g. (c) Out-coupling coefficient calculated as described in Fig. 4 as a function of Λ_g. For both simulation and experiment, the nanocavity depth and width are fixed to $d = 90\,\text{nm}$ and $w = 80\,\text{nm}$.

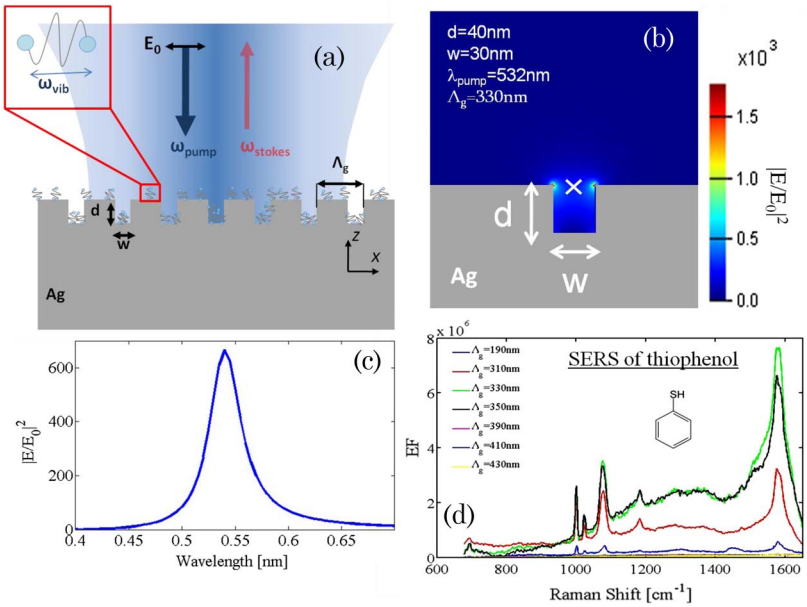

Fig. 9. (Color online) (a) Schematic of the SERS experiment in a silver plasmonic nanocavity gratings. An incident pump beam is focused on the structure via a 20× microscope objective. The Raman scattered light, collected back via the same objective, is filtered and measured with a spectrometer. (b) Example of the intensity distribution of the pump beam (532 nm) at the double resonance condition. (c) Simulation of the resonance for the same parameters as in (b). (d) Experimental measurements of the SERS signal from an adsorbed monolayer of benzenethiol on plasmonic nanocavity gratings for various Λ_g.

surface, the structure is dipped for half a day into the benzenethiol solution immediately after the e-beam evaporation. Measurements were performed immediately after removing the structure from the benzenethiol solution. Figure 9(b) is an example of an FDTD simulation showing the pump intensity distribution in the vicinity of a plasmonic nanocavity grating in silver for parameters fulfilling the previously discussed double resonance condition considering an incident pump wavelength of 532 nm. In this case, this condition occurs for $d = 40\,\text{nm}$, $\Lambda_g = 330\,\text{nm}$ (we also choose $w = 30\,\text{nm}$). The corresponding spectrum is shown in Fig 9(c). Figure 9(b) shows the intensity distribution at this double resonance condition and shows that molecules placed at the entrance of the grooves experience maximum local intensity enhancement, about $\eta^2_{\lambda=532\,\text{nm}} > 1.5 * 10^3$. For small Raman shift, both the pump and the Stokes electric fields are enhanced in the nanocavities and by essentially the identical factor given the vicinity of the Stokes and pump frequencies, leading to a rough estimation of the maximum SERS enhancement $\text{EF} = \eta^4$ of about $2.25 * 10^6$. Figure 9(d) presents the experimental enhancement of the Raman scattering signal as a function of Raman shift in wavenumbers for several Λ_g and for a fixed depth $d = 40\,\text{nm}$. The experimental enhancement of the Raman signal is determined by normalizing the Raman signal obtained from the nanocavity grating with that of a pure benzenethiol solution taking into account the number of molecules in each case [19]. A maximum surface enhanced Raman signal—about $8 * 10^6$—occurs for the period $\Lambda_g = 330\,\text{nm}$. As it has been often reported in similar SERS experiments [20], the measured enhancement is higher than the one expected using field enhancement as the unique mechanism for Raman signal enhancement. Chemical effects, which have been reported to be on the order of 10^2, can explain the mismatch between our measurements and the numerical simulations [21] and also explain the broad underlying continuum in SERS signal observed in Fig. 9(c) around $1300\,\text{cm}^{-1}$ wavenumber. The maximum SERS enhancement occurs for a grating period for $\Lambda_g = 330\,\text{nm}$, but it remains high for slightly larger period than the one providing the maximum $\eta_{\lambda=532\,\text{nm}}$ because even for small Raman shift, the best compromise for both pump and Stokes enhancement ($\eta^2_{\text{pump}}\eta^2_{\text{Stokes}}$) have to be considered. We also notice that no Raman signal is observed when the incident polarization is chosen parallel to the grooves axis.

4. Conclusion

We demonstrated that a metallic film patterned with periodically arranged resonant nanocavities can enhance both degenerate 4 WM and Raman scattering processes by several orders of magnitude. We expect that this technique is broadly applicable to other nonlinear processes, such as second and third harmonic generation, and linear processes such as absorption and fluorescence. Further investigation of nonlinear optical processes at the nanoscale may lead to the development of highly sensitive nonlinear spectroscopy techniques such as surface-enhanced stimulated Raman scattering and coherent anti-stokes Raman scattering.

M. O. S. and P. G. acknowledge National Science Foundation (NSF) Grant No. EEC-0540832, the U. S. Office of Naval Research (ONR),

and the Robert A. Welch Foundation (A-1261). The Harvard University work was supported by the NSF Nanoscale Science and Engineering Center, the Center for Nanoscale Systems at Harvard University, a member of the National Nanotechnology Infrastructure Network, and the Institute for Quantum Studies at Texas A&M University. J. P. T. is supported by the Ecole Normale Superieure de Cachan, France. M. A. K. is supported by the NSF through a Graduate Research Fellowship.

References

1. S. A. Maier, *Plasmonics: Fundamentals and Applications* (Springer, 2007).
2. D. K. Gramotnev and S. I. Bozhevolnyi, "Plasmonics beyond the diffraction limit," Nat. Photon. **4**, 83–91 (2010).
3. J. A. Schuller, E. S. Barnard, W. Cai, Y. C. Jun, J. S. White, and M. L. Brongersma, "Plasmonics for extreme light concentration and manipulation," Nat. Mater. **9**, 193–204 (2010).
4. H-I Peng and B. L. Miller, "Recent advancements in optical DNA biosensors: exploiting the plasmonic effects of metal nanoparticles," Analyst **136**, 436–447 (2011).
5. J. N. Anker, W. P. Hall, O. Lyandres, N. C. Shah, J. Zhao, and R. P. van Duyne, "Biosensing with plasmonic nanosensors," Nat. Mater. **7**, 442–453 (2008).
6. A. Bouhelier, M. Beversluis, A. Hartschuh, and L. Novotny, "Near-field second-harmonic generation induced by local field enhancement," Phys. Rev. Lett. **90**, 013903 (2003).
7. M. Lippitz, M. A. van Dijk, and M. Orrit, "Third-harmonic generation from single gold nanoparticles," Nano Lett. **5**, 799–802 (2005).
8. M. Danckwerts and L. Novotny, "Optical frequency mixing at coupled gold nanoparticles," Phys. Rev. Lett. **98**, 026104 (2007).
9. S. Kim, J. Jin, Y. J. Kim, I. Y. Park, Y. Kim, and S. W. Kim, "High-harmonic generation by resonant plasmon field enhancement," Nature **453**, 757–760 (2008).
10. J. Renger, R. Quindant, N. Van Hulst, and L. Novotny, "Surface-enhanced nonlinear four-wave mixing," Phys. Rev. Lett. **104**, 046803 (2010).
11. P. Genevet, J. P. Tetienne, E. Gatzogiannis, R. Blanchard, M. A. Kats, M. O. Scully, and F. Capasso, "Large enhancement of nonlinear optical phenomena by plasmonic nanocavity gratings," Nano Lett. **10**, 4880–4883 (2010).
12. S. Coyle, M. C. Netti, J. J. Baumberg, M. A. Ghanem, P. R. Birkin, P. N. Bartlett, and D. M. Whittaker, "Confined plasmons in metallic nanocavities," Phys. Rev. Lett. **87**, 176801 (2001).
13. H. T. Miyazaki and Y. Kurokawa, "Controlled plasmon resonance in closed metal/insulator/metal nanocavities," Appl. Phys. Lett. **89**, 211126 (2006).
14. T. Takano and J. Hamasaki, "Propagating modes of a metal-clad-dielectric-slab waveguide for integrated optics," IEEE J. Quantum Electron. **QE-8**, 206–212 (1972).
15. R. W. Boyd, *Nonlinear Optics*, 3rd ed. (Academic, 2008).
16. H. J. Lezec, A. Degiron, E. Devaux, R. A. Linke, L. Martin-Moreno, F. J. Garcia-Vidal, and T. W. Ebbesen, "Beaming light from a subwavelength aperture," Science **297**, 820–822 (2002).
17. N. Yu, J. Fan, Q. Wang, C. Pflugl, L. Diehl, T. Edamura, M. Yamanishi, H. Kan, and F. Capasso, "Small-divergence semiconductor lasers by plasmonic collimation," Nat. Photon. **2**, 564–570 (2008).
18. L. Feng, A. Mizrahi, S. Zamek, Z. Liu, V. Lomakin, and Y. Fainman, "Metamaterials for enhanced polarization conversion in plasmonic excitation," ACS Nano **5**, 5100–5106 (2011).
19. E. C. Le Ru, E. Blackie, M. Meyer, and P. G. Etchegoin, "SERS enhancement factors: a comprehensive study," J. Phys. Chem. C **111**, 13794–13803 (2007).
20. H. KO, S. Singamaneni, and V. V. Tsukruk, "Nanostructured surfaces and assemblies as SERS media," Small **4**, 1576–1599 (2008).
21. A. M. Michaels, M. Nirmal, and L. E. Brus, "Surface enhanced Raman spectroscopy of individual Rhodamine 6G molecules on large Ag nanocrystals," J. Am. Chem. Soc. **121**, 9932–9939 (1999).